Materials Advances

ROYAL SOCIETY OF CHEMISTRY

PAPER

View Article Online
View Journal | View Issue

Cite this: *Mater. Adv.*, 2025, 6, 8657

Defect engineered nickel oxide nanorods by low energy nitrogen ion exposure for supercapacitor applications

Arpita Patro, [a] Satyanarayan Dhal, *[a] Manoj K. Rajbhar, [c] Durga Madhab Pani, [c] Shyamal Chatterjee, [c] Sithara Radhakrishnan [b] and Chandra Sekhar Rout *[b]

Received 9th June 2025,
Accepted 3rd October 2025

DOI: 10.1039/d5ma00613a

rsc.li/materials-advances

This work presents a comprehensive study on the enhancement of electrochemical performance in nickel oxide (NiO) nanorods *via* 5 keV low-energy nitrogen ion (N^+) irradiation. The thin films of nickel oxide nanorods were irradiated at four different ion fluences of 1×10^{16}, 3×10^{16}, 5×10^{16} and 7×10^{16} ions cm^{-2}. The ion irradiation induces surface modifications, including the formation of defects and oxygen vacancies, which significantly improve the nanorods' surface activity and ion transport properties. Electrochemical analyses such as cyclic voltammetry (CV), galvanostatic charge–discharge (GCD), and electrochemical impedance spectroscopy (EIS) confirm that the irradiated samples demonstrate superior specific and areal capacitance, enhanced rate capability, and improved cycling stability compared to pristine NiO. Structural and defect analyses through SRIM, IRADINA and TRI3DYN simulations further support the role of ion-induced modifications in boosting electrochemical behavior. These results highlight nitrogen ion irradiation as an effective technique for tailoring NiO nanostructures toward high-performance supercapacitor applications.

1. Introduction

In recent years, supercapacitors have emerged as critical components in next-generation energy storage technologies due to their high power density, fast charge–discharge capability, and long cycle life.[1,2] Supercapacitor (SC) performance is greatly influenced by the structural, morphological, and compositional characteristics of transition metal oxide-based electrodes. For instance, RuO_2 is an ideal pseudocapacitive electrode material due to its high capacitance, conductivity, and stability, but its high cost limits large-scale applications.[3] Similarly, MnO_2 is a promising, eco-friendly electrode material with high capacitance, but its poor conductivity and slow ion transport limit its supercapacitor performance.[4] Furthermore, V_2O_5 is attractive for supercapacitors due to its multivalent states, abundance, and high capacitance, enabling wide voltage windows and high energy density in both symmetric and asymmetric configurations.[5] Altering the surface of metal oxide electrode materials is a crucial strategy for improving their capacitance. For instance, S. Zallouz[6] *et al.* showed that tuning Co_3O_4 nanoparticle morphology *via* temperature control enhances conductivity and capacitance, outperforming bulk forms for supercapacitor electrodes. Similarly, A. Chouchaine[7] *et al.* demonstrated that Fe_3O_4 nanoparticles synthesized using the SDS surfactant showed enhanced and stable capacitance due to particle size and shape effects, making them promising for energy storage applications.

Among the various electrode materials explored, transition metal oxides, particularly nickel oxide, have attracted considerable interest owing to their high theoretical capacitance, environmental friendliness, and cost-effectiveness. Nickel oxide exhibits excellent pseudocapacitive behaviour arising from surface redox reactions involving Ni^{2+}/Ni^{3+} transitions.[8,9] Nanostructured forms of NiO,[10] such as nanoparticles, nanorods, and nanosheets, offer large surface area and short diffusion paths, which are favourable for rapid ion transport and improved electrochemical performance.[11] However, the electrochemical activity of pristine NiO is often limited by poor electrical conductivity and a relatively small number of accessible active sites.[12] Defect engineering has proven to be a powerful strategy to overcome these limitations by enhancing surface reactivity, electrical conductivity, and ion diffusion kinetics.[13] Among the techniques available, ion beam irradiation stands out as a clean, controllable, and versatile

[a] *Centurion University of Technology and Management, Odisha, India. E-mail: satyanarayan.dhal@cutm.ac.in*
[b] *Centre for Nano and Material Sciences, Jain (Deemed-to-be University), Jain Global Campus, Kanakapura, Bangalore-562112, Karnataka, India. E-mail: r.chandrasekhar@jainuniversity.ac.in, csrout@gmail.com*
[c] *School of Basic Sciences, Indian Institute of Technology Bhubaneswar, Bhubaneswar 752050, India*

tool to modify the surface structure and introduce defects such as vacancies and interstitials without altering the bulk composition.[14,15] Controlled ion bombardment induces defect formation, surface roughening, and morphological restructuring,[16] all of which contribute to improved surface area, ion accessibility, and charge transfer capabilities. These structural modifications can enhance conductivity and provide more electrochemically active sites, making ion-irradiated transition metal oxides highly promising for next-generation energy storage applications. Thus, combining morphology engineering with ion beam techniques can yield high-performance SC electrodes with superior capacitance, energy density, and cycle life. Low-energy ion irradiation enables surface-level modifications that are highly relevant for tuning nanostructured electrode behaviour.[17] Despite its potential, the application of low-energy ion irradiation to tailor the properties of NiO nanostructures for supercapacitor applications remains underexplored. Most prior studies have focused on irradiation effects in optical[18] systems, with limited correlation to electrochemical performance enhancement. The central novelty of this research is the deliberate creation of junctions between individual NiO nanorods using a low-energy N^+ ion beam. While ion irradiation is known to create surface defects, this study demonstrates its unique application in inducing localized, defect-assisted "welding" at the contact points of adjacent nanorods. This process leads to the formation of stable Y-shaped connections and complex network-like structures, a significant morphological evolution from the original isolated nanorods. This controlled fusion of nanorods into a cohesive network offers two key advantages: (1) enhanced surface area – the transformation into a 3D network creates a more open architecture. This significantly increases the electrochemically accessible surface area compared to the pristine film, where many nanorod surfaces might be physically blocked or electronically isolated; (2) increased active sites – the irradiation process not only forms junctions but also generates a high density of surface defects and oxygen vacancies, which act as additional electrochemically active sites for faradaic reactions.

Ultimately, this junction-induced enhancement of the active surface area is directly responsible for the observed improvements in supercapacitor performance, leading to higher specific and areal capacitance, superior rate capability, and improved charge transfer kinetics in the irradiated samples.

In this work, we report the surface modification of hydrothermally synthesized NiO nanorods by 5 keV N^+ ion irradiation at four different fluences (1×10^{16}, 3×10^{16}, 5×10^{16} and 7×10^{16} ions per cm^2). We investigate the structural, morphological, and defect evolution through XRD, Raman spectroscopy, FESEM, and Monte Carlo-based simulations (TRIM,[19] IRADINA,[20] TRI3DYN[21]). The formation of nanorod junctions, increase in surface defects, and local stoichiometric shifts are correlated with their potential to enhance electrochemical activity for supercapacitor applications.

2. Experimental details

2.1. Synthesis

Nickel oxide (NiO) nanorods were synthesized using a hydrothermal technique at 200 °C (Fig. 1). In a typical procedure, 0.47 g of $NiCl_2{\cdot}6H_2O$ was dissolved in a mixture of 32 mL of ethylene glycol and 18 mL of deionized (DI) water. The solution was stirred magnetically at room temperature to ensure homogeneity. Subsequently, 0.12 g of sodium oxalate ($Na_2C_2O_4$) was

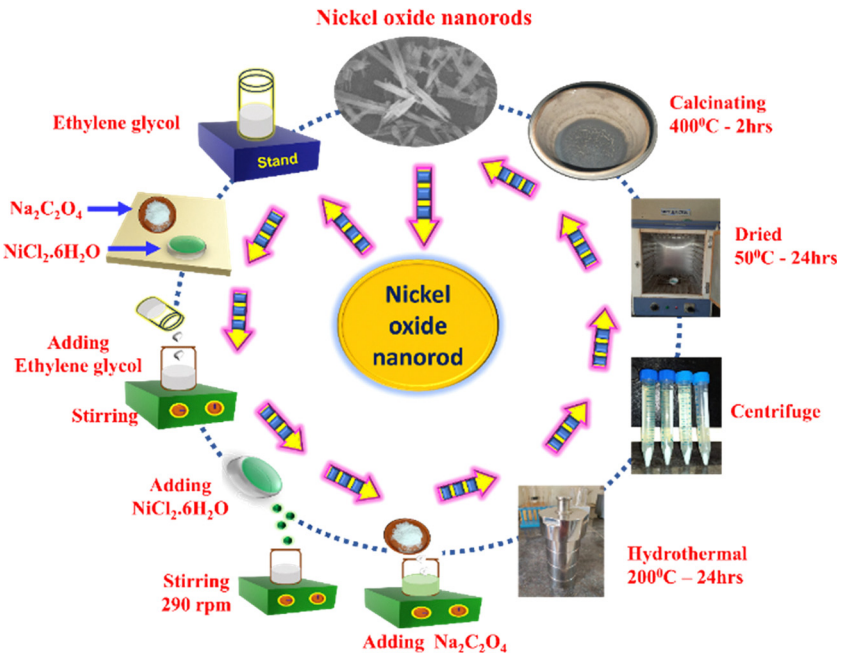

Fig. 1 Schematic diagram of the synthesis of nickel oxide nanorods using a hydrothermal method.

added to the solution and stirring was continued for one hour to achieve uniform distribution of Ni^{2+} ions.[22]

The resulting precursor solution was transferred to a 100 mL Teflon-lined stainless-steel autoclave and maintained at 200 °C for 24 hours. After the reaction, the autoclave was naturally cooled to room temperature. The resulting precipitate was separated *via* centrifugation, washed five times alternately with ethanol and DI water to remove impurities, and then air-dried at 50 °C for 24 hours. The obtained light blue-green precursor material, identified as $NiC_2O_4{\cdot}2H_2O$, was subsequently calcined at 400 °C for 2 hours in air to obtain polycrystalline NiO nanorods.

The synthesized NiO nanorod solution was spin-coated onto pre-cleaned, ultrasonicated silicon substrates using a spin coater operating at 2000 rpm for uniform thin film formation.

Ion irradiation was performed using 5 keV N^+ ions at a fluence of 1×10^{16}, 3×10^{16}, 5×10^{16} and 7×10^{16} ions per cm^2. The irradiation experiments were conducted using a custom-designed ion–matter interaction chamber installed at IIT Bhubaneswar.

Morphological analysis of pristine and irradiated samples was carried out using a Zeiss Ultra field emission scanning electron microscope (FESEM) to observe the structure, diameter, and surface evolution of the nanorods. The crystalline structure was investigated using X-ray diffraction (XRD) on a PANalytical X'Pert Pro diffractometer with Cu Kα radiation (λ = 1.5406 Å), operating in the 2θ range of 20°–80°. Raman spectroscopy was performed using a T64000 micro-Raman spectrometer (Jobin Yvon) in backscattering geometry to probe vibrational modes and defect formation in the NiO nanostructures. The Wuhan Corrtest electrochemical workstation (CS350, version 5.3) was used to conduct all the electrochemical measurements using a traditional three-electrode system.

3. Results and discussion

Fig. 2(a) presents a plan-view FESEM image of pristine nickel oxide (NiO) nanorods at low magnification (1 μm), revealing a uniform distribution of nanorods across the substrate surface. The NiO nanorods exhibit consistent alignment and coverage. The average diameter and length of the nanorods were estimated to be 80 ± 10 nm and nearly 0.9 ± 1 μm. Fig. 2(b) shows a high-magnification image (100 nm), providing a closer view of the nanorod morphology and confirming the diameter of individual nanorods to be approximately 95 nm, with well-defined one-dimensional geometry and smooth surfaces. Fig. 2(c–f) display the plan-view FESEM images of nickel oxide

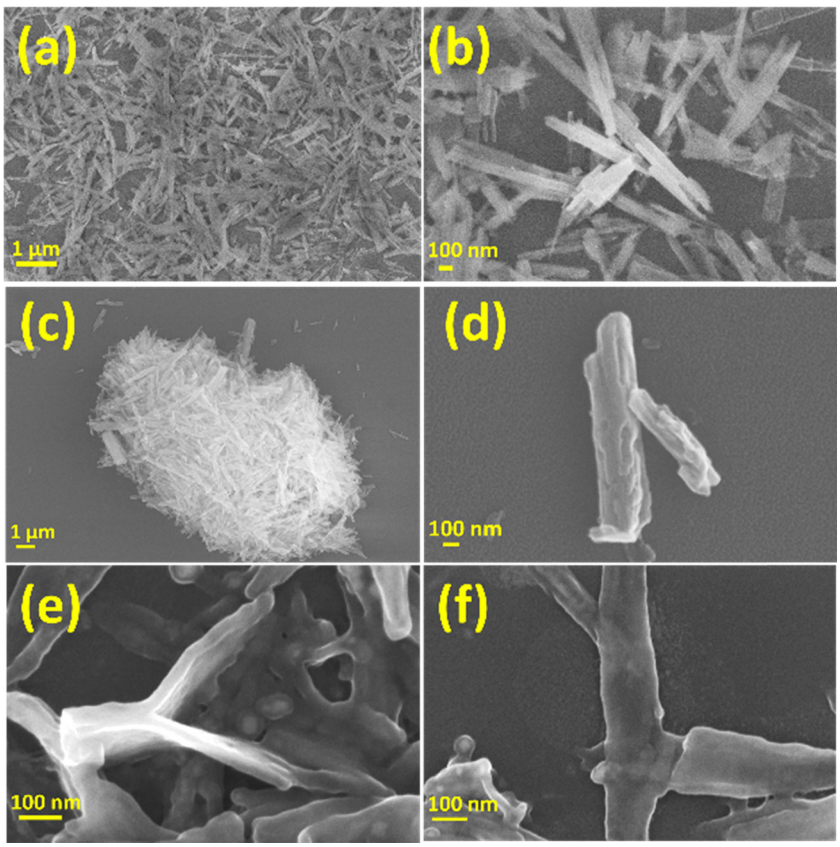

Fig. 2 Plan-view field emission scanning electron microscopy image of the as-deposited nickel oxide nanorods coated on a Si substrate (a) at low magnification and (b) at high magnification. Joining of nickel oxide nanorods after N^+ irradiation at 5 keV and a fluence of 1×10^{16} ions per cm^2 (c) at low magnification, (d) initial joining at low magnification, and junction formation (e) at a fluence of 5×10^{16} ions per cm^2 and (d) at a fluence of 7×10^{16} ions per cm^2.

(NiO) nanorods irradiated with 5 keV N^+ ions at a fluence of 1×10^{16} ions per cm^2, 5×10^{16} ions per cm^2, and 7×10^{16} ions per cm^2. Fig. 2(c) and (d) show the images at a fluence of 1×10^{16} ions per cm^2, captured at low and high magnifications, respectively. The images reveal the initial stages of nanorod joining.[23] Two individual nanorods begin to merge, forming small aggregates (Fig. 2(d)). The discrete nanorod geometry is noticeably altered, suggesting partial coalescence and defect-assisted bonding between neighbouring nanorods induced by the ion beam. Fig. 2(e) and (f) show the NiO nanorods irradiated at a higher fluence of 5×10^{16} ions per cm^2 and 7×10^{16} ions per cm^2, respectively. These images clearly exhibit extensive junction formation.

A significant morphological change is observed post-irradiation, where Y-connections develop between nanorods.[24] The nanorods appear to be interconnected, forming network-like structures, which are significantly different from the isolated morphology of the pristine sample.

Fig. 3 shows the FESEM images of irradiated NiO nanorods captured at high magnification, *i.e.* 20 nm. The image reveals that after irradiation at a higher fluence of 5×10^{16} ions per cm^2 there is clear joining (shown by yellow dotted lines) between the nanorods, resulting in a loss of crystallinity, which led to amorphization of the material.

The observed joining behaviour is attributed to ion-induced defect generation, where vacancies and interstitials are formed unevenly across the nanorod surface. This defect distribution promotes atomic migration and bonding at contact points, leading to structural fusion and network formation, particularly at higher fluences.

3.1. Microstructural characterization

The crystal structures of the pristine and nitrogen ion irradiated nickel oxide nanorods were investigated using XRD. The XRD spectrum (Fig. 4) shows the characteristic peaks of the rhombohedral crystal structure of NiO. The peaks at 37.90°, 44.10°, 64.50°, and 77.70° are attributed to the [111], [020], [022], and [222] planes (COD: 1010093). Due to irradiation, a decrease in peak intensity is observed from pristine to

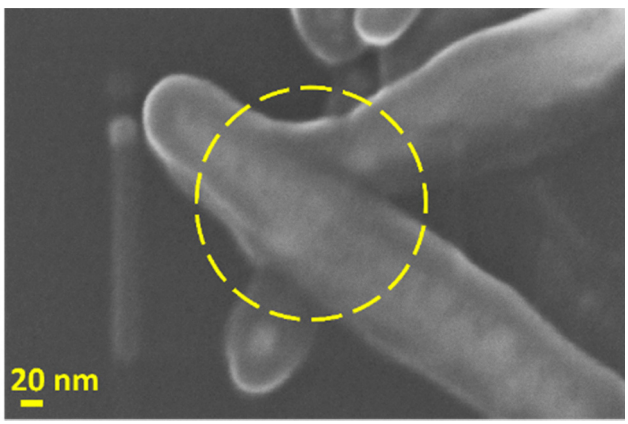

Fig. 3 Joining between two nanorods after N^+ irradiation at 5 keV at a fluence of 5×10^{16} ions per cm^2, showing clear amorphization.

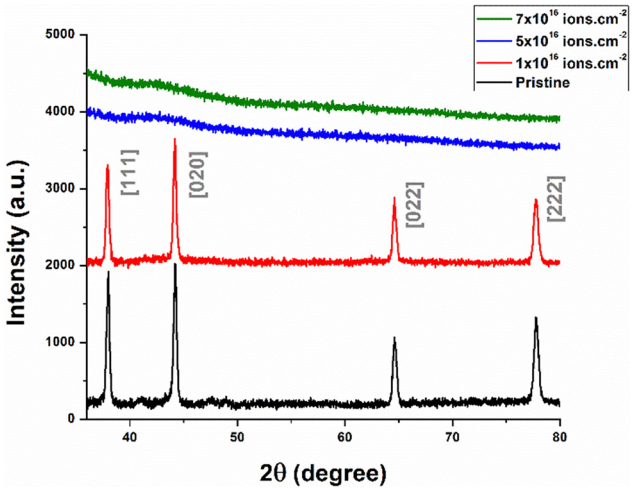

Fig. 4 X-ray diffractograms of pristine nanorods (black), irradiated nickel oxide nanorods with fluences and irradiated nickel oxide nanorods at fluences of 1×10^{16} (red), 5×10^{16} (blue), and 7×10^{16} (green) ions per cm^2.

1×10^{16} ions per cm^2 due to the loss of crystallinity in the nanorods. At higher fluences (5×10^{16} and 7×10^{16} ions cm^{-2}), the intensity of peaks diminished, indicating amorphization. To visualize the effect of ion irradiation on nickel oxide nanorods, we conducted simulations using SRIM[19] and IRADINA,[20] where many parameters were estimated by modeling the passage of energetic nitrogen ions through the target material using the Monte-Carlo approach.

Fig. 5 presents a comprehensive analysis of the interaction between 5 keV nitrogen (N^+) ions and nickel oxide (NiO) nanorods using TRIM[25] (Transport of Ions in Matter) simulations, highlighting how low-energy ion irradiation induces defect formation and energy deposition near the surface of the nanostructure.

Fig. 5(a) shows a 3D map of the ion trajectories through the NiO nanorod layer and into the silicon substrate. The N^+ ions exhibit a shallow penetration profile, consistent with their low energy (5 keV), with most trajectories confined within ~8 nm (~80 Å) of the NiO layer. The visualization reflects multiple scattering events and lateral spread within the upper portion of the material, emphasizing that the surface region is the primary site of interaction and modification. The black line marks the NiO–Si interface. This localized energy transfer leads to significant atomic displacements (79) and defect formation near the surface, including approximately 77 vacancies and 2 replacements per ion (Fig. 5(b)). The lateral and projected straggle distribution (Fig. 5(c)) illustrates that the lateral spread of ion-induced defects is comparable to the depth range, promoting inhomogeneous damage and facilitating the formation of network structures through junctions between nanorods. TRIM simulations predicted that the ions deposit about 3.49 keV per ion energy at a distance of 8 nm across a nanorod. The energy deposition profile (Fig. 5(d)) shows that the majority of the incident ion energy is absorbed by nickel and oxygen atoms in the NiO layer, with minimal energy reaching the underlying silicon substrate. These observations

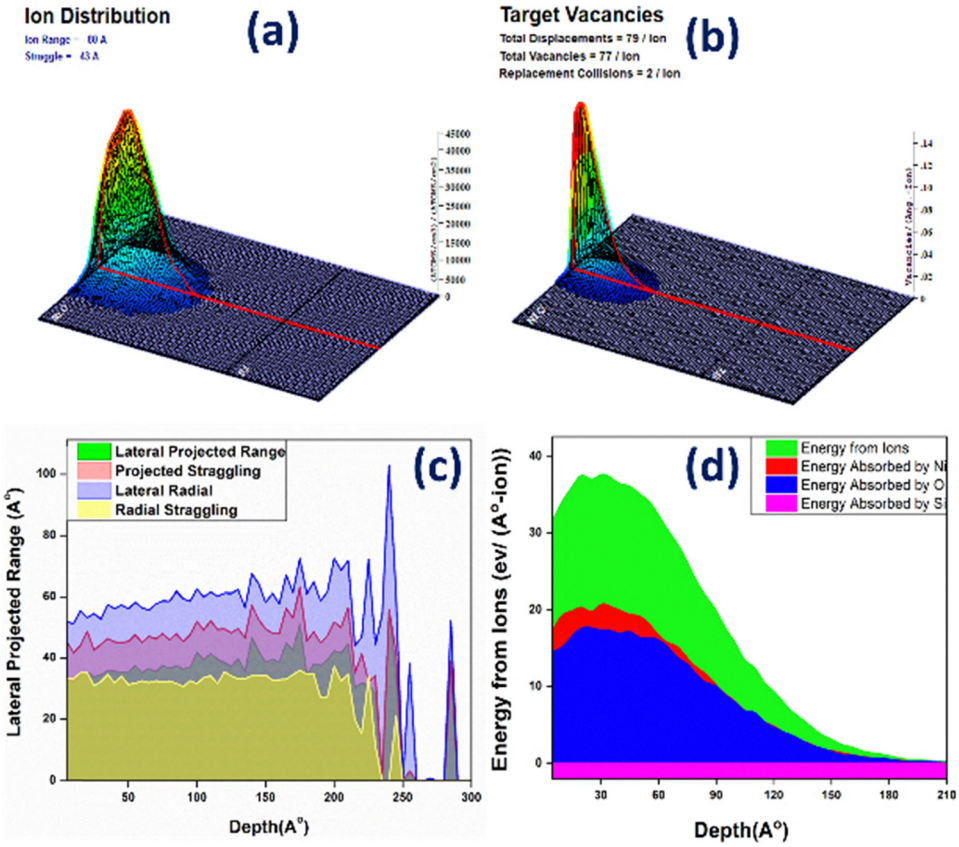

Fig. 5 TRIM simulation: ion distribution (a), energy from the ions (N^+) and the amount of energy absorbed by nickel, oxygen and silicon (b), lateral projected range (c), and the number of total displacements, vacancies and replacements for 5 keV nitrogen ions exposed to nickel oxide nanorods (d).

support the experimental findings of nanorod coalescence, surface oxygen depletion, and enhanced redox activity, indicating that controlled ion irradiation can be a powerful tool to engineer surface defects and improve the electrochemical performance of NiO nanorods for supercapacitor applications.

IRADINA simulations were employed to model the effects of nitrogen ion implantation into nickel oxide (NiO) nanorods, offering a detailed understanding of ion–solid interactions within nanostructures. The simulation was conducted on a nanorod with a diameter of 90 nm, irradiated by 5 keV N^+ ions at a fluence of 3×10^{16} ions per cm^2 under normal incidence. For computational efficiency, only a thin slice of the nanorod was modelled, with periodic boundary conditions (PBC) applied along the *z*-axis to mimic translational symmetry. The slice was divided into a grid of 90×90 cells, each measuring 1 nm $\times$ 1 nm, resulting in a total of 8100 cells for analysis. The simulations revealed a non-uniform implantation profile, attributed to the lateral confinement of the nanorod, which increases the probability of ions exiting the side of the structure. The estimated ion range at this energy ($\sim$10 nm) is significantly smaller than the nanorod's diameter, highlighting surface localization effects.

Fig. 6(a) shows a schematic diagram of how ions strike the nickel oxide nanorod. The direction of the N^+ ion beam towards

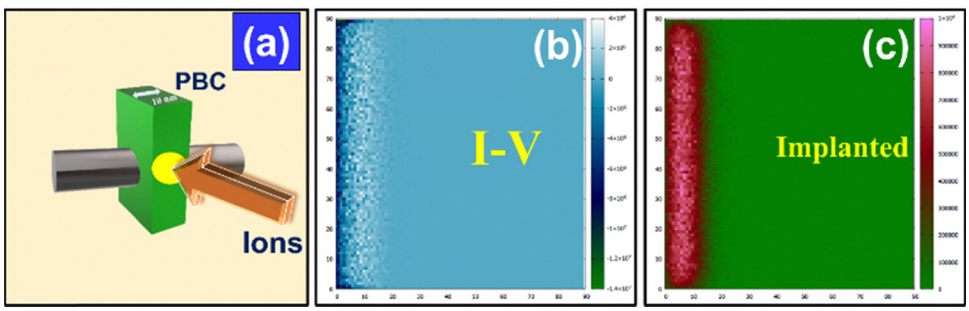

Fig. 6 (a) Schematic diagram of IRADINA simulations, (b) excess interstitials minus excess vacancies (arb. units; teal: excess interstitials, white: excess vacancies), and (c) number of implanted ions shown in magenta (arb. units).

the *x*-axis is illustrated, with the nanorod depicted in grey and the PBC set at 10 nm. The arrow denotes the ion beam direction. Fig. 6(b and c) show the cross-sectional view of the rod. Fig. 6(b) presents a map of residual damage calculated as the difference between excess interstitials and excess vacancies within each cell. Areas with an excess of interstitials are shown in teal, while those with an excess of vacancies are shown in white, indicating a concentration of vacancies in the peripheral regions of the nanorods. This effect is more pronounced at the sides compared to the upper surface, with the maximum vacancy concentration reaching approximately 4×10^6. Fig. 6(c) visualizes the distribution of implanted ions (sum of interstitials and replacements) within the nanorods, where magenta regions correspond to higher ion counts and green regions to lower counts. The implanted ion count reaches approximately 1×10^6 in arbitrary units. These excess vacancies and interstitials contribute to bending moments within the nanorods, a phenomenon further corroborated by complementary 3D simulations capturing dynamic structural evolution under ion irradiation.

The effects of very low energy ion irradiation on nanorods were investigated using TRI3DYN[21] simulations. TRI3DYN simulations showed the changes in the atomic percentages and defects of the nanorods before and after ion bombardment. The binary collision approximation (BCA) in the Monte Carlo method serves as the foundation for TRI3DYN simulations.

Fig. 7 (top) presents the 3D view of two different nickel oxide nanorods oriented in a parallel direction. Here the atomic densities are represented on a scale of 10^{24} cm^{-3}. The volume of the entire box (Fig. 7a–f) is estimated by 3D voxels having a size of $40 \times 80 \times 80$ nm^3 ($x \times y \times z$ nm^3). The as-deposited nickel oxide nanorods are shown in purple colour with a scale of 0.5.

Fig. 7(a and b) show the results of TRI3DYN simulations illustrating the atomic fraction changes of oxygen and nickel in nickel oxide (NiO) nanorods after irradiation with 5 keV N^+ ions at a fluence of 8×10^{15} ions per cm^2. Fig. 7(a) displays the oxygen atomic fraction across the nanorod surface. A visible colour shift from purple (0.5) to red ($\sim$0.3) near the top surface indicates a depletion of oxygen atoms after irradiation. This preferential sputtering of lighter oxygen atoms is consistent with surface reduction effects induced by ion bombardment. Fig. 7(b) shows the corresponding nickel atomic fraction, where the colour changes from purple ($\sim$0.5) to blue ($\sim$0.7) at the irradiated surface. This reflects a relative enrichment of nickel atoms due to the preferential loss of oxygen. These results suggest that the surface of the NiO nanorods becomes Ni-rich and oxygen-deficient upon low-energy ion exposure.

Fig. 7(c–f) illustrate the atomic fraction changes of oxygen and nickel in nickel oxide (NiO) nanorods under 5 keV nitrogen (N^+) ion irradiation, simulated using TRI3DYN. The simulations were carried out at two different ion fluences: 1×10^{16} ions per cm^2 (Fig. 7(c) and (d)) and 3×10^{16} ions per cm^2 (Fig. 7(e) and (f)). Fig. 7(c) and (e) present the oxygen atomic fraction for the two fluences. The surface colour gradually shifts from purple ($\sim$0.5) to red ($\sim$0.3 or lower) with increasing fluence, clearly indicating enhanced oxygen loss at higher ion doses. This is attributed to preferential sputtering of lighter oxygen atoms. Fig. 7(d) and (f) show the corresponding nickel atomic fraction, with the colour shifting from purple ($\sim$0.5) to blue ($\sim$0.7 or higher). This reflects a relative enrichment of nickel at the irradiated surface due to oxygen depletion.

Higher fluence (3×10^{16} ions per cm^2) causes greater stoichiometric imbalance, deeper defect penetration, and more intense atomic restructuring of the nanorods. These structural modifications contribute to enhanced electrochemical behaviour by increasing the number of active sites, surface area, and defect-driven conductivity, all favourable for supercapacitor applications.

Fig. 8 shows the cross-sectional view of two as-deposited (pristine) nickel oxide (NiO) nanorods, highlighting the oxygen atomic fraction distribution, as simulated using TRI3DYN. The nanorods exhibit two circular profiles, corresponding to the realistic nanorod geometry. The colour scale ranges from red (lower atomic fraction) to blue (higher atomic fraction), with the pristine nanorods showing a uniform blue coloration throughout. This indicates a consistent oxygen atomic fraction of $\sim$0.5 across the entire cross-section, confirming stoichiometric uniformity and no surface degradation prior to ion irradiation. This baseline plot serves as a reference for comparing with irradiated samples, where deviations from uniformity (*e.g.*, colour changes near the surface) indicate oxygen depletion or preferential sputtering. Fig. 8 illustrates the oxygen atomic fraction in the cross-sectional views of two nickel oxide (NiO) nanorods after irradiation with 5 keV N^+ ions at two different fluences: 8×10^{15} ions per cm^2 (Fig. 8(b)) and 3×10^{16} ions per cm^2 (Fig. 8(c)). The simulations were carried out using TRI3DYN, and the atomic fraction is visualized on a colour scale ranging from blue (0.5) to red (0.0). At 8×10^{15} ions per cm^2, a clear depletion of oxygen is observed at the top surface and junction interface between nanorods, visible as red and yellow regions, indicating oxygen atomic fractions dropping below 0.3. At 3×10^{16} ions per cm^2, the oxygen loss is more pronounced and extends more deeply into the nanorods, with wider red zones on both the upper surface and at the nanorod interface. This suggests enhanced sputtering and recoil of oxygen atoms due to higher ion impact density. These results support the interpretation that oxygen is preferentially sputtered during irradiation, leading to surface oxygen vacancies, Ni-rich outer layers, and potential joining at nanorod junctions due to the bonding induced by high defect density. Such modifications are critical for enhancing electrochemical activity in supercapacitor applications, as they increase the density of redox-active sites and conductive pathways. Increasing fluence results in more severe oxygen depletion at the top surface and inter-nanorod junction, visible as red and yellow zones. These changes indicate the formation of oxygen vacancies and enhanced structural modification, correlating with the observed network formation and expected improvements in electrochemical behaviour.

Fig. 9 displays the cross-sectional maps of atomic defects in two NiO nanorods after 5 keV N^+ ion irradiation, simulated using TRI3DYN. The images present the spatial distribution of

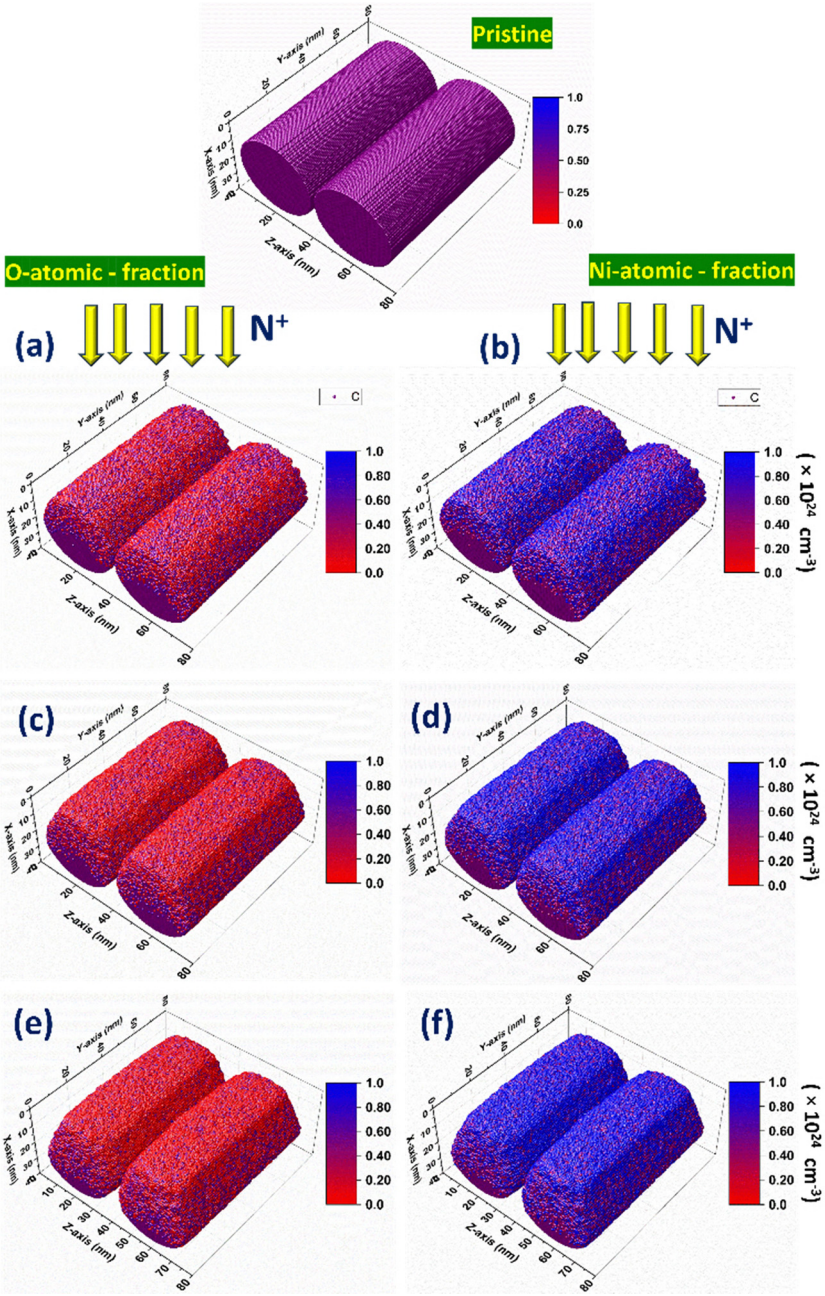

Fig. 7 3D view showing two pristine nickel oxide nanorods oriented in the parallel direction (top). Atomic fractions of (a) oxygen and (b) nickel after N^+ ion irradiation at 5 keV at a fluence of 8×10^{15} cm^{-2}; oxygen atomic fraction and nickel atomic fraction for two different nickel oxide nanorods when irradiated with 5 keV N^+ ions at a fluence of 1×10^{16} cm^{-2} (c) and (d) and 3×10^{16} cm^{-2} (e) and (f), respectively.

recoiled oxygen and nickel atoms as a function of ion fluence. Fig. 9(a) and (b) show the oxygen atomic defects at 8×10^{15} ions per cm^2 and 3×10^{16} ions per cm^2, respectively. Fig. 9(c) and (d) show the nickel atomic defect distributions at the same fluences. At lower fluence, a moderate number of oxygen recoils are observed near the surface (green–yellow zone), while at higher fluence, the oxygen vacancy concentration intensifies (orange–red zone) and penetrates more deeply into the nanorod structure. Nickel atoms show fewer displacements overall compared to oxygen (as expected due to higher atomic mass). However, at 3×10^{16} ions per cm^2, there is a notable increase in nickel displacement, with the defect region extending from the surface toward the centre, indicated by the transition from red to blue across the cross-section. These results confirm that oxygen atoms are preferentially sputtered, especially in the surface and junction regions, consistent with earlier atomic fraction analysis. High fluence irradiation causes significant atomic disruption, promoting defect clustering, junction fusion, and network formation—critically influencing surface chemistry and energy storage performance.

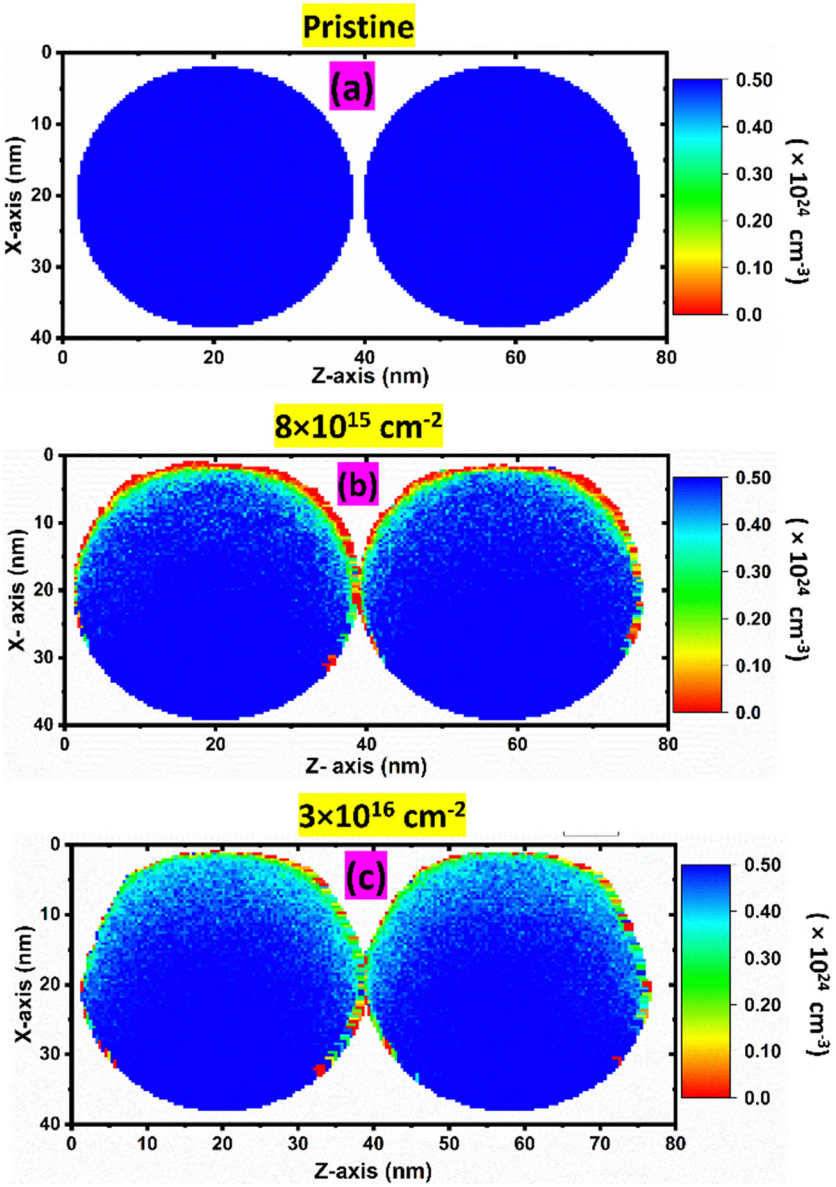

Fig. 8 (a) Cross-sectional view of two as-deposited nickel oxide (NiO) nanorods showing the oxygen atomic fraction distribution, as simulated by TRI3DYN. The uniform blue color across the nanorods corresponds to an oxygen atomic fraction of 0.5, confirming stoichiometric uniformity in the pristine (unirradiated) state; TRI3DYN-simulated cross-sectional views showing oxygen atomic fraction distribution in two NiO nanorods irradiated with 5 keV N^+ ions at different fluences: (b) 8×10^{15} ions per cm^2 and (c) 3×10^{16} ions per cm^2.

Raman spectroscopy serves as a powerful, non-destructive technique to probe the internal structure, bonding, and vibrational properties of nanomaterials, including nickel oxide (NiO) nanorods. In this study, Raman measurements were conducted on both pristine and irradiated NiO samples to elucidate the effects of ion irradiation-induced defects on their vibrational characteristics (Fig. 10). The Raman spectra provide distinct "fingerprints" that provide detailed insights into the crystallinity, phase composition, structural disorder, and defect density of the samples.[26] These findings corroborate the defect formation mechanisms predicted by TRIM, IRADINA, and TRI3DYN simulations and support the role of controlled ion irradiation in enhancing the electrochemical performance of NiO nanorods for supercapacitor applications. The spectrum of the pristine (unirradiated) NiO sample, shown in black, exhibits the characteristic features of crystalline nickel oxide.[27] A strong, well-defined peak is observed at approximately 540–550 cm^{-1}. This peak is identified as the one-phonon longitudinal optical (1LO)[28] mode, which arises from the primary Ni–O bond vibrations within the NiO crystal lattice.[29–31] The spectrum also shows a broad, low-intensity feature rising towards the higher wavenumber region ($\sim$700–900 cm^{-1}).[32] This region typically contains weaker, second-order phonon modes, such as the two-transverse optical (2TO) mode, and potentially two-magnon (2M) scattering, which is a signature of the antiferromagnetic ordering in NiO. Overall, the sharp and

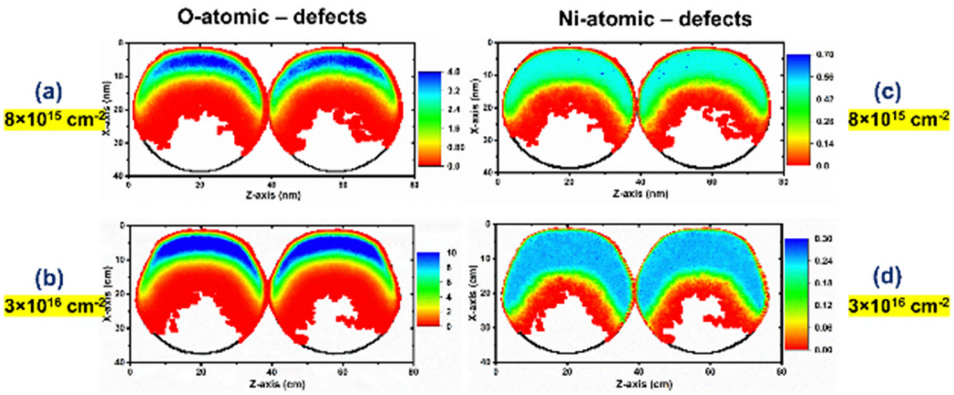

Fig. 9 Oxygen atomic defects at (a) 8×10^{15} cm^{-2} and (b) 3×10^{16} cm^{-2} and nickel atomic defects at (c) 8×10^{15} cm^{-2} and (d) 3×10^{16} cm^{-2}.

intense 1LO peak confirms the good crystalline quality of the pristine NiO sample. The subsequent spectra show a clear and systematic evolution of the NiO structure as a function of increasing nitrogen ion fluence. The primary effect observed is the progressive degradation of the crystalline structure due to irradiation-induced damage. At a fluence of 1×10^{16} ions per cm^2 (red line), the intensity of the 1LO peak is dramatically reduced. This significant drop in intensity indicates that the ion bombardment has introduced a substantial number of lattice defects, disrupting the long-range order of the crystal.

Interestingly, at a fluence of 3×10^{16} ions per cm^2 (blue line), the intensity of the 1LO peak is slightly recovered compared to the 1×10^{16} sample. At the higher fluence (magenta line), the characteristic 1LO peak has almost completely vanished, replaced by a very broad, low-intensity hump. This indicates severe lattice damage and the loss of most of the crystalline structure. The material is transitioning into a highly disordered or amorphous-like state. The spectrum for the highest fluence (green line) is essentially a flat line with no discernible peaks. This complete suppression of the Raman signal signifies the amorphization of the NiO surface layer. The long-range periodic arrangement of atoms has been destroyed by the extensive ion bombardment, eliminating the conditions necessary for coherent phonon scattering. A decrease in the 1LO mode intensity is specifically associated with the formation of defects like Ni vacancies induced by the irradiation process.

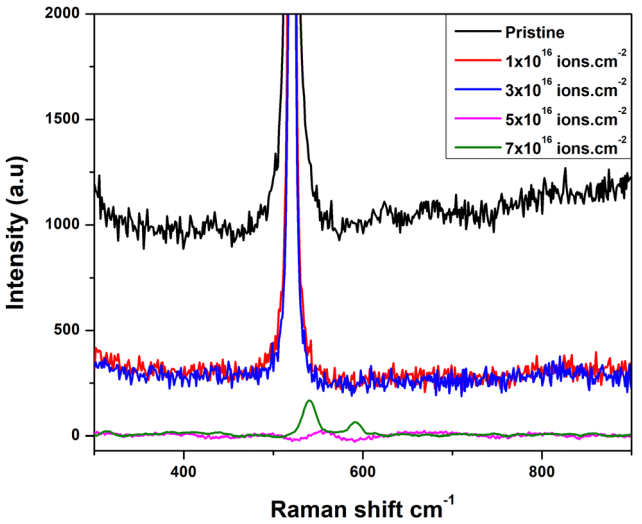

Fig. 10 Raman spectra of NiO nanorods irradiated with 5 keV N^+ ions at fluences of 1×10^{16} ions per cm^2 (red curve), 3×10^{16} ions per cm^2 (blue curve), 5×10^{16} ions per cm^2 (magenta curve) and 7×10^{16} ions per cm^2 (green curve), showing vibrational modes.

3.2. Electrochemical measurements

Given the strong evidence from multiple characterization (XRD and Raman) and simulation (TRI3DYN and IRADINA) techniques, we concluded that the samples irradiated at 5×10^{16} and 7×10^{16} ions cm^{-2} were not viable candidates for enhanced supercapacitor performance. Therefore, we focused our comprehensive electrochemical testing on the sample that demonstrated an optimized level of defect engineering without sacrificing the essential crystalline structure, corresponding to a fluence of 3×10^{16} ions cm^{-2}. The electrochemical performance of pristine nickel oxide (NiO) nanorods was systematically investigated using cyclic voltammetry (CV), galvanostatic charge–discharge (GCD), and electrochemical impedance spectroscopy (EIS). The cyclic voltammetry (CV) curves of pristine and ion-irradiated nickel oxide (NiO) samples were recorded at a scan rate of 20 mV s^{-1} in a potential window of −0.2 to 0.6 V (Fig. 11(a)). The irradiated sample exhibits a notably higher current response compared to the pristine one, indicating enhanced electrochemical activity. The CV loops for both samples display quasi-rectangular shapes with distinct redox peaks, confirming pseudocapacitive behaviour dominated by surface faradaic reactions involving Ni^{2+}/Ni^{3+} transitions.[33] The broader and more intense CV curve of the irradiated sample suggests an increase in available active sites, improved electron transfer kinetics, and greater electrochemically accessible surface area, likely due to defect engineering induced by ion irradiation. As the scan rate increases (Fig. 11(b)), the CV curves broaden and exhibit a progressive shift in the redox peak positions due to polarization effects and increasing resistance to ion transport. Notably, the area enclosed by the CV curves grows with increasing scan rate,

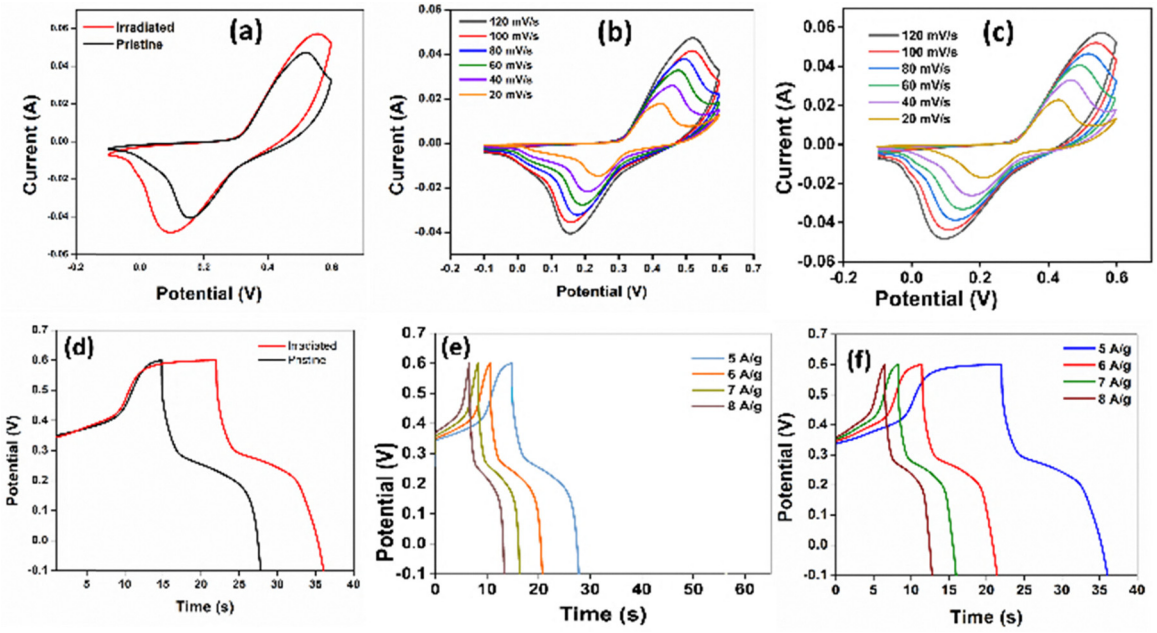

Fig. 11 Cyclic voltammetry curves of nickel oxide nanorods comparing pristine and irradiated samples (a); at varying scan rates for pristine (b) and irradiated (c) samples; constant current charge discharge curves for both pristine and irradiated samples of nickel oxide nanorods (d); with variation in current density for pristine (e) and irradiated (f) samples. All the irradiated graphs correspond to a fluence (optimum) of 3×10^{16} ions per cm^2.

reflecting an enhancement in current response. However, the relative peak broadening and decreased sharpness at higher scan rates suggest diffusion limitations and slower kinetics of faradaic processes. These observations indicate that the pristine NiO nanorods possess a robust pseudocapacitive behaviour with good rate capability but may benefit from surface modifications, such as ion irradiation, to further enhance their electrochemical performance. Similarly, the cyclic voltammograms (CVs) of the irradiated NiO nanorods were recorded at scan rates of 20, 40, 60, 80, 100, and 120 mV s^{-1} over the potential range of −0.2 to 0.6 V (Fig. 11(c)). The CV profiles maintain the characteristic pseudocapacitive shape with clear redox peaks corresponding to the Ni^{2+}/Ni^{3+} redox couple. As the scan rate increases, the current response becomes broader, with a slight shift in peak potentials, suggesting good rate capability. The observed increase in peak current with the scan rate indicates enhanced kinetics of charge storage and efficient ion transport, which can be attributed to the defect engineering induced by nitrogen ion irradiation. The galvanostatic charge–discharge (GCD) curves of pristine and irradiated NiO nanorods, recorded at a constant current density, illustrate the differences in electrochemical performance between the two samples (Fig. 11(d–f)). The irradiated sample exhibits a longer discharge time and a more symmetric triangular profile compared to the pristine sample, indicative of improved charge storage capacity and enhanced reversibility. The potential drop at the onset of discharge is reduced for the irradiated sample, reflecting lower internal resistance and better conductivity, likely resulting from defect-induced pathways for charge transport. The extended plateau region in the irradiated sample's discharge curve suggests a higher specific capacitance and improved energy storage capability. The GCD curves for pristine NiO nanorods at varying current densities of 4, 5, 6, 7, and 8 A g^{-1} (Fig. 11(d)) provide key insights into the material's rate capability and charge storage performance. At lower current densities (*e.g.*, 4 A g^{-1}), the discharge curves display long, nearly symmetrical triangular profiles with extended plateau regions, indicative of high specific capacitance and efficient charge storage. As the current density increases, the discharge time progressively decreases, and the curves become less linear and more distorted, reflecting reduced ion diffusion efficiency and increased internal resistance. The shortening of discharge times and increased *IR* drop at higher currents highlight the kinetic limitations of pristine NiO at high rates. These findings suggest that while pristine NiO demonstrates good performance at low current densities, its rate capability may be significantly enhanced by introducing structural defects or surface modifications, such as ion irradiation. The GCD curves of irradiated NiO nanorods at current densities ranging from 5 to 8 A g^{-1} (Fig. 11(d)–(f)) reveal substantial improvements in rate capability and charge storage performance compared to the pristine sample. At low current densities (*e.g.*, 5 A g^{-1}), the discharge profile is extended and maintains a nearly ideal triangular shape, indicating excellent capacitance and reversibility. As the current density increases, the discharge time decreases, as expected, but the curves remain relatively linear and less distorted than those of the pristine sample, demonstrating improved ion diffusion kinetics and reduced internal resistance. The diminished *IR* drop and prolonged discharge times at higher current densities highlight the role of nitrogen ion irradiation in creating surface defects and enhancing electron transport pathways.

3.3. Electrokinetic analysis of charge storage

To gain deeper insight into the charge storage kinetics of the pristine NiO nanorods, an electrokinetic analysis was performed to quantify the capacitive and diffusion-controlled contributions. The total current at a fixed potential can be separated into contributions from surface capacitive effects (k_1v) and diffusion-controlled processes ($k_2v^{1/2}$).

To further elucidate the charge storage mechanism and compare the kinetics of the pristine and irradiated samples, the capacitive and diffusion-controlled contributions were quantified from the CV data at various scan rates. Fig. 12 presents a comparative bar chart of the percentage of charge stored *via* capacitive processes for both electrodes.

A clear trend is observed for both samples: the contribution from capacitive storage systematically increases with the scan rate. This confirms that at higher charge–discharge rates, the fast, surface-controlled capacitive processes become the dominant mechanism over the slower, diffusion-limited processes.

More importantly, a direct comparison reveals the positive effect of nitrogen ion irradiation. The irradiated sample consistently exhibits a higher percentage of capacitive charge storage over the entire range of scan rates. For instance, at a high rate of 0.12 V s^{-1}, the capacitive contribution increases from approximately 82% in the pristine sample to over 83.5% in the irradiated sample. This enhancement, while modest, is significant. It provides quantitative proof that the ion-induced surface defects successfully created additional, highly accessible redox-active sites. These new sites improve the surface kinetics, allowing for more efficient charge storage, especially at high rates. This kinetic advantage helps explain the superior rate capability and higher specific capacitance observed for the irradiated electrode throughout the electrochemical analysis.

The variation of specific capacitance with applied current density for pristine and irradiated NiO nanorods is presented in Fig. 13(a). Both samples exhibit a characteristic decrease in specific capacitance as the current density increases, attributed to limited ion accessibility and diffusion at higher rates. However, the irradiated sample consistently demonstrates higher specific capacitance values across all current densities compared to the pristine counterpart. At 5 A g^{-1}, the specific capacitance of the irradiated sample reaches approximately 70 C g^{-1}, compared to 66 C g^{-1} for the pristine sample. The variation of areal capacitance with current density for pristine and irradiated NiO nanorods is illustrated in Fig. 13(b). The irradiated sample consistently exhibits higher areal capacitance values across all current densities, indicating enhanced electrochemical performance. At a current density of 0.5 mA cm^{-2}, the irradiated sample shows an areal capacitance of approximately 6.5 F cm^{-2}, compared to 2.8 F cm^{-2} for the pristine sample. As the current density increases, the areal capacitance of both samples decreases due to limited ion diffusion and increased resistive losses. However, the irradiated sample retains superior capacitance values even at higher current densities, demonstrating improved rate capability. This enhancement can be attributed to the formation of surface defects and improved conductivity resulting from nitrogen ion irradiation, which facilitates more efficient charge transfer and ion transport in the electrode material.

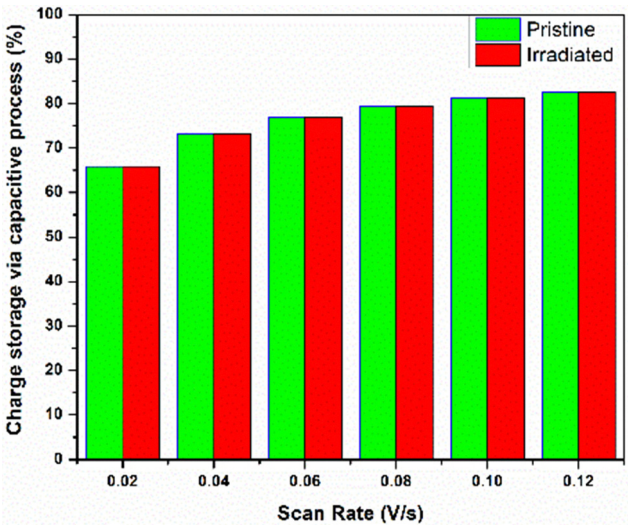

Fig. 12 Comparative analysis of the charge storage kinetics for pristine and irradiated NiO nanorods.

The cycling stability of pristine and irradiated NiO nanorods was evaluated over 5000 cycles, as illustrated in Fig. 13(c and d). The specific capacitance and coulombic efficiency were monitored as functions of the cycle number. Both samples exhibit stable cycling behavior, with the irradiated sample demonstrating superior specific capacitance and coulombic efficiency throughout the test period. The irradiated sample maintains a higher specific capacitance, which indicates enhanced charge storage capability and structural integrity after prolonged cycling. Coulombic efficiency, a measure of charge–discharge reversibility, is consistently higher in the irradiated sample, confirming improved electrochemical stability and reduced degradation. All these results emphasize the beneficial role of nitrogen ion irradiation in enhancing the cycling performance and durability of NiO nanorods for long-term supercapacitor applications.

The electrochemical impedance spectroscopy (EIS) data for pristine and irradiated NiO nanorods, represented by the Nyquist plots (Fig. 13e) and bar graphs (Fig. 13f), provide key insights into their charge transport properties. The Nyquist plots exhibit a typical semicircular shape in the high-frequency region, followed by a linear segment at low frequencies, characteristic of charge-transfer and diffusion-controlled processes, respectively. The irradiated sample displays a smaller semicircle compared to the pristine sample, indicating a reduction in charge-transfer resistance (R_{ct}) from 25.8 Ω to 9.5 Ω, as shown in the bar chart. Additionally, the irradiated sample exhibits a lower series resistance (R_s), decreasing from 11.4 Ω to 8.8 Ω, reflecting enhanced electrical conductivity and ion transport pathways introduced by nitrogen ion irradiation. These improvements in resistance parameters confirm that ion irradiation effectively reduces charge-transfer barriers and improves the overall electrochemical performance of NiO

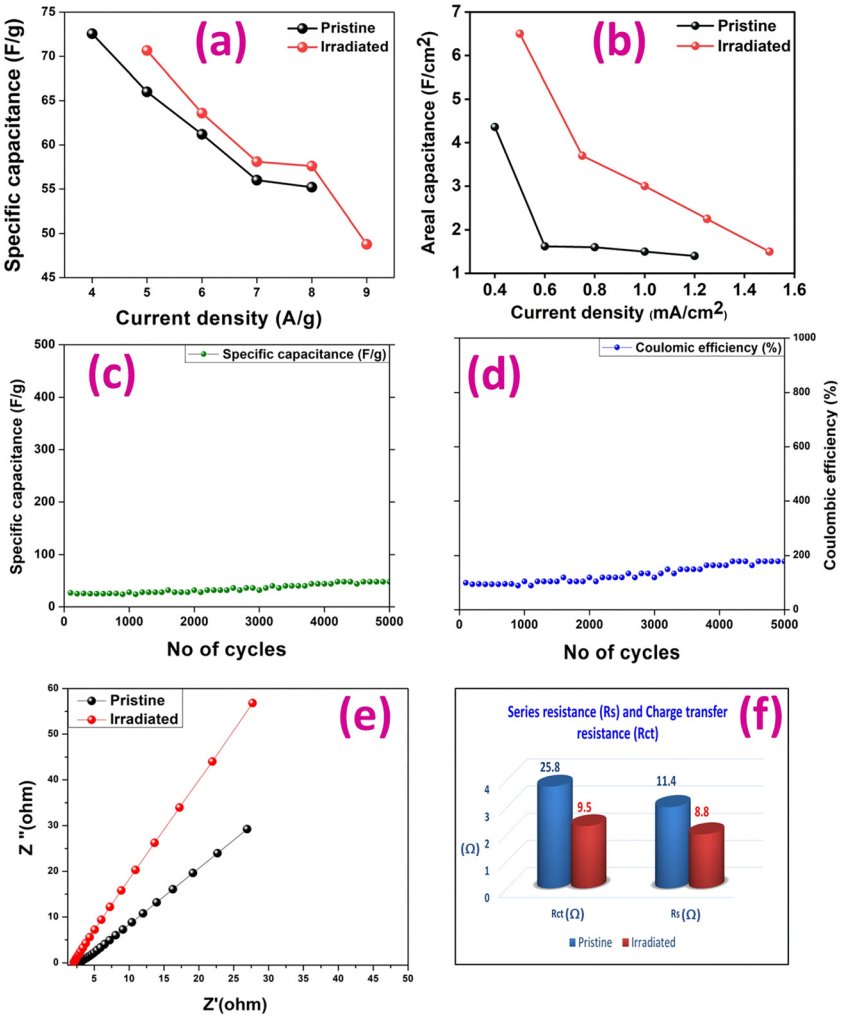

Fig. 13 Applied current density with capacitance variation for both pristine and irradiated samples of nickel oxide nanorods: (a) specific capacitance and (b) areal capacitance; (c) and (d) capacitance stability of the electrode evaluated over 5000 continuous charge–discharge cycles; (e) Nyquist plots of pristine and irradiated NiO nanorods illustrating complex impedance behavior, with the irradiated sample showing a smaller semicircle corresponding to lower charge-transfer resistance. (f) Bar chart comparing the series resistance (R_s) and charge-transfer resistance (R_{ct}) values for pristine and irradiated samples, highlighting reductions in both resistances due to nitrogen ion irradiation.

Table 1 Comparison of various NiO nanostructured materials (with different structures) with the corresponding areal capacitance

Electrode material (morphology and composition)	Areal capacitance (F cm^{-2})	Ref.
Ultrathin NiO nanoflakes on Ni foam	0.87	34
MOF-derived hierarchical-porous NiO film	2.08	35
NiO nanosheets on Ni foam	1.98	36
N^+ irradiated NiO nanorods	6.5	Current work

nanorods, further validating its suitability for high-performance supercapacitor applications. To understand the impact of morphology on electrochemical performance, the areal capacitance of various NiO nanostructured materials is compared (Table 1).

This work demonstrates a powerful defect engineering strategy using a low-energy ion irradiation technique for the rational design of high-performance electrode materials. The findings provide a clear pathway for tuning the properties of nanostructured oxides for energy storage. This versatile approach can be readily extended to other material systems to develop next-generation, high-performance electrodes.

4. Conclusions

In conclusion, this study demonstrates the enhancement in the electrochemical performance of NiO nanorods achieved through nitrogen ion irradiation. Ion-induced surface modifications result in increased active sites, improved electrical conductivity, and enhanced ion transport, as evidenced by cyclic voltammetry, galvanostatic charge–discharge, and electrochemical impedance spectroscopy analyses. The irradiated samples exhibit higher specific and areal capacitance, superior rate capability, and better cycling stability compared to pristine samples. Structural characterization, supported by SRIM and

IRADINA simulations, reveals that irradiation-induced defects and oxygen vacancies play a critical role in modifying the nanorod surfaces, contributing to enhanced charge storage performance. These findings establish low-energy ion irradiation as an effective strategy to optimize NiO-based materials for advanced supercapacitor applications.

Author contributions

Arpita Patro: conceptualization and manuscript writing – original draft; Satyanarayan Dhal: overall analysis and manuscript preparation; Chandra Sekhar Rout: review; Manoj K. Rajbhar: irradiation measurements and TRI3DYN simulation measurements; Durga Madhab Pani: electrochemical characterization; Shyamal Chatterjee: review; Sithara Radhakrishnan: electrochemical characterization.

Conflicts of interest

There are no conflicts to declare.

Data availability

The data supporting the study's conclusions will be available from the corresponding author upon reasonable request.

Acknowledgements

The authors are thankful to Prof. Wolfhard Moller, HZDR, Germany for the support of the TRI3DYN program and to Dr P. Karmakar, Variable Energy Cyclotron Centre (VECC), Kolkata for assistance with irradiation at high fluence.

References

1 S. Natarajan, M. Ulaganathan and V. Aravindan, *J. Mater. Chem. A*, 2021, **9**, 15542–15585.
2 R. Chakraborty, K. Vilya, M. Pradhan and A. Nayak, *J. Mater. Chem. A*, 2022, **13**, 6965–7005.
3 F. Yu, L. Pang and H.-X. Wang, *Rare Met.*, 2021, **40**, 440–447.
4 P. B. Liu, Y. D. Zhu, X. G. Gao, Y. Huang, Y. Wang, S. Y. Qin and Y. Q. Zhang, *Chem. Eng. J.*, 2018, **350**, 79–88.
5 D. Chen, J. Li and Q. Wu, *J. Nanopart. Res.*, 2019, **21**, 201.
6 S. Zallouz, B. Réty, L. Vidal, J. M. Le Meins and C. Matei Ghimbeu, *ACS Appl. Nano Mater.*, 2021, **4**, 5022–5037.
7 R. S. Kate, S. A. Khalate and R. J. Deokate, *J. Alloys Compd.*, 2018, **734**, 89–111.
8 A. Sasmal and A. Nayak, *J. Energy Storage*, 2023, **58**, 106342.
9 T. F. Yi, T. T. Wei, J. Mei, W. Zhang, Y. Zhu, Y. G. Liu, S. Luo, H. Liu, Y. Lu and Z. Guo, *Adv. Sustainable Syst.*, 2020, **4**, 1900137.
10 S. H. S. Pai, S. K. Pandey, E. J. J. Samuel, J. U. Jang, A. K. Nayak and H. Han, *J. Energy Storage*, 2024, **76**, 109731.
11 R. A. Patil, C. P. Chang, R. S. Devan, Y. Liou and Y. R. Ma, *ACS Appl. Mater. Interfaces*, 2016, **8**, 9872–9880.
12 R. Paulose, R. Mohan and V. Parihar, *Nano-Struct. Nano-Objects*, 2017, **11**, 102–111.
13 W. Lu, L. Yan, W. Ye, J. Ning, Y. Zhong and Y. Hu, *J. Mater. Chem. A*, 2022, **10**, 15267–15296.
14 L. Huang, H. Wu, G. Cai, S. Wu, D. Li, T. Jiang, B. Qiao, C. Jiang and F. Ren, *ACS Nano*, 2024, **18**, 2578–2610.
15 A. Patro, C. S. Rout, S. Dhal and S. Chatterjee, *Nanotechnology*, 2025, **36**, 212001.
16 S. Dhal, S. Chatterjee and S. Chatterjee, *AIP Conf. Proc.*, 2017, **1832**, 1.
17 W. Guo, W. Wei, H. Zhu, Y. Hu, H. Jiang and C. Li, *eScience*, 2023, **3**, 100082.
18 N. A. Althubiti, A. Atta, N. Al-Harbi, R. K. Sendi and M. M. Abdelhamied, *Opt. Quantum Electron.*, 2023, **55**, 348.
19 J. F. Ziegler, M. D. Ziegler and J. P. Biersack, *Nucl. Instrum. Methods Phys. Res., Sect. B*, 2010, **268**, 1818–1823.
20 J. P. Crocombette and C. Van Wambeke, *EPJ Nucl. Sci. Technol.*, 2019, **5**, 7.
21 W. Möller, *Nucl. Instrum. Methods Phys. Res., Sect. B*, 2014, **322**, 23–33.
22 K. Nguyen, N. D. Hoa, C. M. Hung, D. T. T. Le, N. Van Duy and N. Van Hieu, *RSC Adv.*, 2018, **8**, 19449–19455.
23 S. Dhal, P. Das, A. Patro, M. Swain, S. R. Hota, D. Sahu and S. Chatterjee, *Radiat. Phys. Chem.*, 2021, **188**, 109649.
24 A. Patro, M. K. Rajbhar, S. Chatterjee, A. Patra, C. S. Rout and S. Dhal, *J. Alloys Compd.*, 2023, **960**, 170441.
25 S. Dhal, A. Patro, M. Swain and K. Supraja, *IJST*, 2020, **13**, 97.
26 M. Schindler, M. Akbari Alavijeh, M. L. Oliveira and L. F. Silva, *Geostand. Geoanal. Res.*, 2025, **49**, 133–159.
27 E. Aytan, B. Debnath, F. Kargar, Y. Barlas, M. Lacerda, J. X. Li, R. K. Lake, J. Shi and A. A. Balandin. *arXiv*, preprint, arXiv.1710.06386, 2017, DOI: **10.48550/arXiv.1710.06386**.
28 N. Mironova-Ulmane, A. Kuzmin, I. Sildos, L. Puust and J. Grabis, *Latv. J. Phys. Tech. Sci.*, 2019, **56**(2), 61–72.
29 E. Aytan, B. Debnath, F. Kargar, Y. Barlas, M. M. Lacerda, J. X. Li, R. K. Lake, J. Shi and A. A. Balandin, *Appl. Phys. Lett.*, 2017, **111**, 25.
30 N. Mironova-Ulmane, A. Kuzmin, I. Sildos, L. Puust and J. Grabis, *Latv. J. Phys. Tech. Sci.*, 2019, **56**, 61–72.
31 P. Salunkhe, A. A. V. Muhammed and D. Kekuda, *Mater. Res. Express*, 2020, **7**, 016427.
32 A. Sunny and K. Balasubramanian, *J. Phys. Chem. C*, 2020, **124**(23), 12636–12644.
33 B. Maharana, S. Ratha, A. S. Shajahan, B. Chakraborty, R. Jha and S. Chatterjee, *Phys. Rev. Appl.*, 2021, **15**, 034013.
34 H. Xiao, F. Qu and X. Wu, *Appl. Surf. Sci.*, 2016, **360**, 8–13.
35 S. Zhou, S. Wang, S. Zhou, H. Xu, J. Zhao, J. Wang and Y. Li, *Nanoscale*, 2020, **12**(16), 8934–8941.
36 H. Yan, D. Zhang, J. Xu, Y. Lu, Y. Liu, K. Qiu, Y. Zhang and Y. Luo, *Nanoscale Res. Lett.*, 2014, **9**(1), 424.